https://doi.org/10.1016/j.ijepes.2016.05.005

Power and efficiency analysis of high-frequency Wireless Power Transfer Systems

Giulia Di Capua [a,*], Nicola Femia [a], Giovanni Petrone [a], Gianpaolo Lisi [b], Dingkun Du [b], Rajaram Subramonian [b]

[a] Dpt. of Information and Electrical Eng. and Applied Math., University of Salerno, Fisciano, SA, Italy
[b] Kilby Laboratories – Silicon Valley, Texas Instruments Inc., Santa Clara, CA, USA

ARTICLE INFO

Keywords:
Wireless Power Transfer
Losses
Efficiency
System optimization
Wearable applications

ABSTRACT

This paper discusses the losses analysis of low power high-frequency Wireless Power Transfer Systems (WPTSs). Ideal models for efficiency evaluation of WPTS can predict performances that are quite far from the real ones. The model proposed in this paper includes semiconductor devices losses, as well as modulation of duty-cycle and phase for the secondary side rectifier. The global influence of semiconductor devices and control parameters on the overall WPTS performances is numerically determined by solving the herein discussed non linear equations system. Experimental measurements realized on a 2 W@6.78 MHz WPTS demonstrate the validity of this analysis.

Introduction

In the last years, the research on Wireless Power Transfer Systems (WPTSs) experienced a big expansion [1]. WPTSs can be well applied to wirelessly power small wearable or portable electronics [2,3], to contactless charging systems for electric vehicles [4–6], to factory automation systems [7,8], to medical and health care devices [9,10]. Many papers, standards, books, and reports about WPTSs design have been published, each one with a special emphasis on specific applications, different topologies and compensation networks [11–13], resonance frequency and soft-switching [14], system efficiency and power [15,16]. In this regard, WPTSs are often characterized with respect to reference efficiency values given as the ratio between the load power and the total power entering the transmitter loop. Many papers on this subject merely focus on the optimization of the transmitter-receiving modules and experimental efficiency values of WPTSs are only provided [16]. However, comparative discussions on global WPTS optimization, involving silicon devices and control issues impact, are missing. This problem is particular important in WPTSs design for wearable and portable applications, such as mobile phones or smart-watches chargers, where the achievement of high efficiency becomes more and more challenging. In such kind of applications, critical issues are:

- coupling factor between primary transmitting (Tx) coil and secondary receiving (Rx) coil, which is typically much lower than unity in charger application [17];
- load current, which is varying over the battery charge cycle [18];
- restricted and unlicensed lower Industrial Scientific Medical (ISM) band at 6.78 MHz [19];
- fire angles of the controlled rectifier switches used to modulate the rectifier duty-cycle and phase [20–23], in order to improve the WPTS efficiency.

Papers discussing the efficiency benefits of controlled rectifiers and/or post-regulators typically adopt simplified ideal models to characterize WPTSs. A first simplification consists in representing the secondary side rectifier and load simply as a linear resistor. A second simplification lies in neglecting switching losses in the semiconductor devices both of the primary side inverter and of the secondary side controlled rectifier and post-regulators. Such assumptions may yield too optimistic efficiency predictions, especially in high-frequency WPTSs. In this scenario, enhanced models and methods to predict the impact of semiconductor devices switching losses on the WPTS performance are required. Indeed,

* Corresponding author.
E-mail addresses: gdicapua@unisa.it (G. Di Capua), femia@unisa.it (N. Femia), gpetrone@unisa.it (G. Petrone), gianpaolo.lisi@ti.com (G. Lisi), d-du@ti.com (D. Du), raj.subramonian@ti.com (R. Subramonian).

because of the ISM band restrictions, traditional MOSFET technology is approaching its capability limit and it is necessary to evaluate the opportunity to switch to other technologies, like enhancement mode Gallium Nitride (GaN) transistors [24,25]. The open problem is then to analyze the overall influence of semiconductor devices losses on performances of a WPTS. The problem becomes even more involved if the mismatch of the transmitter-to-receiver coupling factor is included, as this one strongly characterizes several applications of large interest beyond portable/wearable devices, such as electric vehicles.

Therefore, the main goal of this paper is to provide an effective model for the power and efficiency analysis of WPTSs. The investigation is focused on low power applications relevant to wearable devices. Nevertheless, concepts, models and methods herein discussed are quite general. Indeed, the same loss investigation can be used for reliable design and optimization of other WPTSs, and extended to other applications like the automotive ones. Section 'WPTS modeling' presents the general analytical model for the calculation of the first harmonic component solution in a WPTS and illustrates a numerical method for the solution of the proposed analytical model. In section 'Loss analysis and experimental verification', the results of the analysis of a 2 W@6.78 MHz WPTS are presented, and then validated with experimental measurements. Finally, section 'MOSFETs impact on WPTS output power and efficiency' discusses the impact of semiconductor devices on WPTS output power and efficiency.

WPTS modeling

All the parameters and the quantities adopted in the proposed modeling are summarized in Table 1. All superscript "*rec*" and "*inv*" are referred to rectifier and inverter elements, respectively.

The WPTS considered in this paper is based on the series compensation architecture shown in Fig. 1. The WPTS is supposed to work with a primary constant frequency and a secondary PWM control ensuring duty-cycle D and phase-shift modulation $\phi = \phi_{I2} - \phi_{V2}$ [26]. In these conditions, the phase modulation involves a phase lag (or a phase lead) with respect to the current zero crossing in the commutations of the rectifier switches. Figs. 2 and 3 show typical current and voltage waveforms for the primary and secondary side of a WPTS.

Such plots exemplify different commutation conditions for the inverter MOSFETs $M_1, \ldots, M_4$ and the rectifier MOSFETs $Q_1, \ldots, Q_4$, given different phase lag/lead ($\phi > 0$ or $\phi < 0$). In this regard, the key issues for the loss analysis of a WPTS are:

- identifying the type of commutations the MOSFETs undergo, depending on α, β and ϕ;
- formulate a specific set of loss formulae for all the possible combinations of commutations, depending on α, β and ϕ.

It is worth to remember that a MOSFET undergoes to a *hard commutation* whenever it changes its state while its drain-to-

Table 1
Main parameters for WPTS and MOSFETs.

Symbols	WPTS main parameters			MOSFETs main parameters		
TX = transmitter	f_s	[Hz]	Switching frequency	R_{dson}	[Ω]	Channel resistance
RX = receiver	$\omega_s = 2\pi f_s$	[rad/s]	Angular frequency	R_g	[Ω]	Gate resistance
I_1 = 1st harm. of TX current	V_{in}	[V]	Input voltage	$R_{gd,on}$	[Ω]	Turn-on gate driver resistance
	V_{bat}	[V]	Battery voltage	$R_{gd,off}$	[Ω]	Turn-off gate driver resistance
V_1 = 1st harm. of TX voltage	R_{bat}	[Ω]	Battery series resistance	R_{sns}	[Ω]	Series sensing resistance
	$V_{out} = V_{bat} + R_{bat} I_{out}$	[V]	Output voltage	R_{ext}	[Ω]	External series gate resistance
I_2 = 1st harm. of RX current	L_1	[H]	TX coil inductances	g_{fs}	[S]	Transconductance
	L_2	[H]	RX coil inductances	C_{oss}	[F]	Output capacitance
V_2 = 1st harm. of RX voltage	Q_{L1}	–	TX coil quality factor at ω_s	Q_g	[C]	Total gate charge
	Q_{L2}	–	RX coil quality factor at ω_s	Q_{gs}	[C]	Gate-source charge
Z_1 = TX coil impedance	$R_{L_1} = \omega_s L_1 Q_{L_1}^{-1}$	[Ω]	TX coil resistance	Q_{gd}	[C]	Gate-drain charge
Z_2 = RX coil impedance	$R_{L_2} = \omega_s L_2 Q_{L_2}^{-1}$	[Ω]	RX coil resistance	Q_{gsw}	[C]	Switching gate charge
α (see Figs. 2 and 3)	K_{12}	–	TX-RX coupling coefficient	Q_{rr}	[C]	Body diode recovery charge
β (see Figs. 2 and 3)	$M = K_{12}\sqrt{L_1 L_2}$	[H]	TX-RX mutual inductance	t_{dt}	[s]	Gate signal dead-time
ϕ (see Figs. 2 and 3)	$C_{s1} = (\omega_s^2 L_1)^{-1}$	[F]	TX resonant capacitor	V_{th}	[V]	Gate-source threshold voltage
$s_\alpha = \sin(\alpha)$	$C_{s2} = (\omega_s^2 L_2)^{-1}$	[F]	RX resonant capacitor	V_{sd}	[V]	Body diode forward voltage
$c_\alpha = \cos(\alpha)$	Q_{C1}	–	TX capacitor quality factor at ω_s	Q_{rr}	[C]	Body diode recovery charge
$s_\beta = \sin(\beta)$	Q_{C2}	–	RX capacitor quality factor at ω_s	V_{dr}	[V]	Driver voltage
$c_\beta = \cos(\beta)$	$R_{C_1} = (\omega_s C_{s1} Q_{C1})^{-1}$	[Ω]	series resistance of TX capacitor	$R_{gon} = R_{gd,on} + R_g + R_{ext}$		
$s_\phi = \lvert\sin(\phi_{V1} - \phi_{I1})\rvert$	$R_{C_2} = (\omega_s C_{s2} Q_{C2})^{-1}$	[Ω]	series resistance of RX capacitor	$R_{goff} = R_{gd,off} + R_g + R_{ext}$		

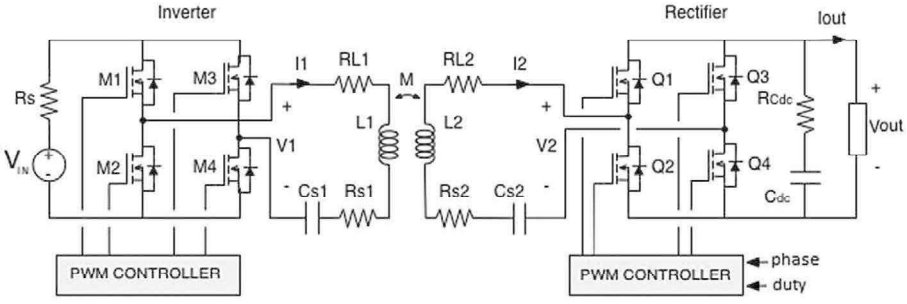

Fig. 1. Series–series resonant WPTS.

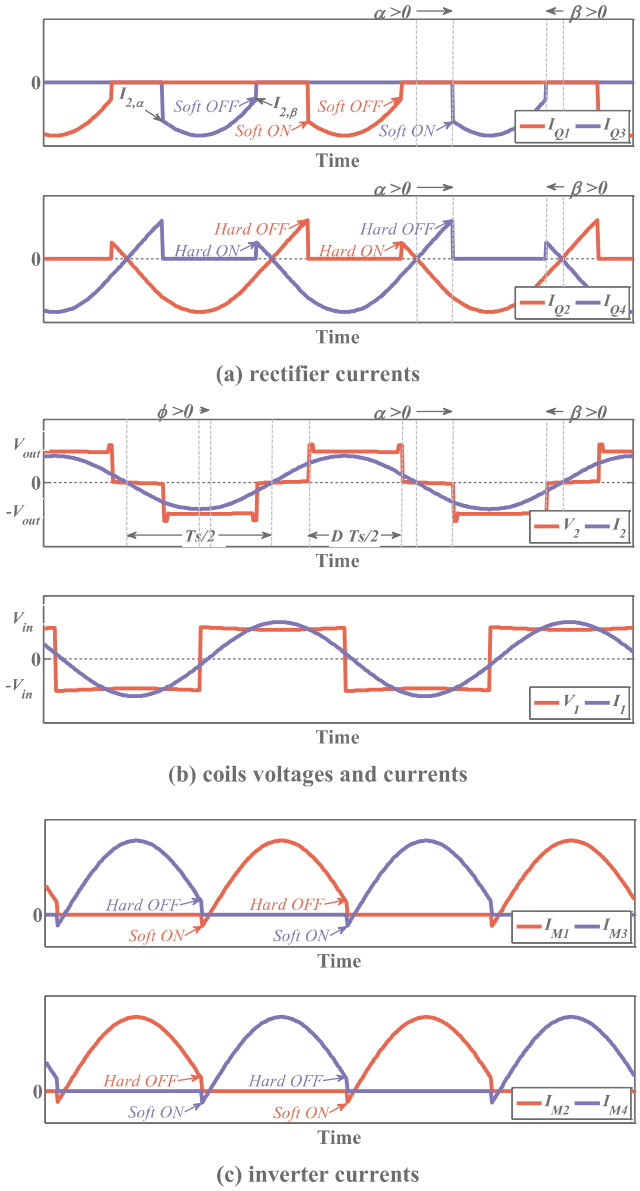

Fig. 2. Primary and secondary side WPTS waveforms ($\alpha > 0$, $\beta > 0$).

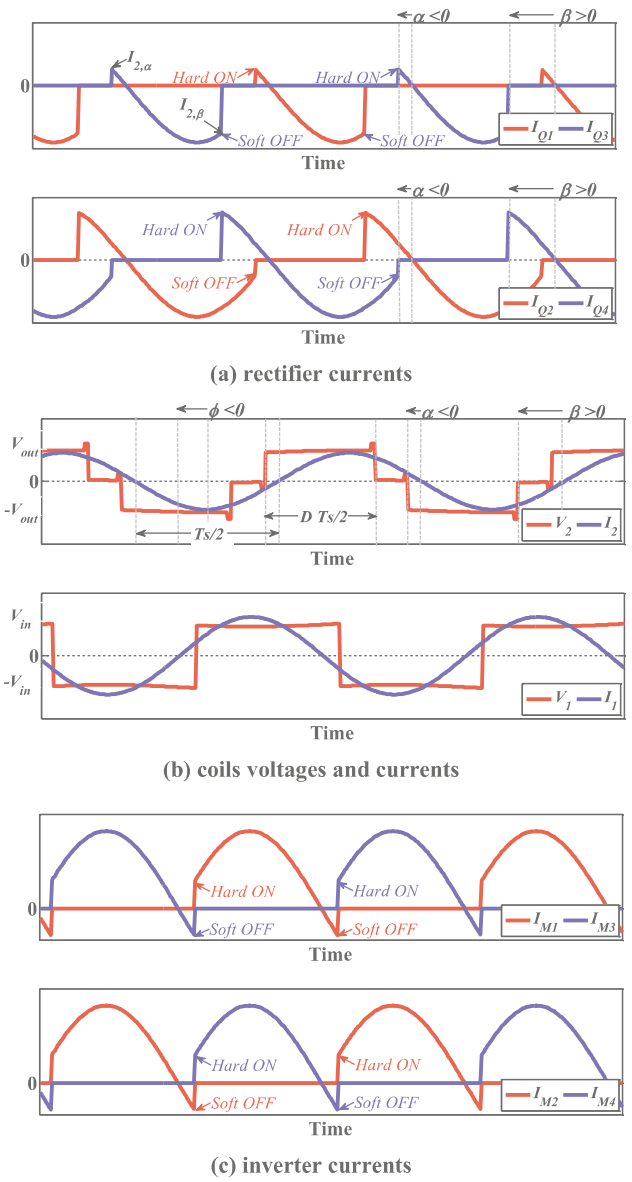

Fig. 3. Primary and secondary side WPTS waveforms ($\alpha < 0$, $\beta > 0$).

source channel current is positive. A MOSFET undergoes to a *soft commutation* whenever it changes its state while its drain-to-source channel current is negative. In the first case, switching losses are much higher. Therefore, hard or soft switching commutations in the inverter and rectifier stages can strongly influence the system output power and efficiency.

Whatever way the WPTS rectifier output is connected to the end load (it can be terminated onto a battery with a device to be powered in parallel, or interfaced to them through a dc/dc post regulator), the general problem to solve is to determine the operable output current I_{out} and the system efficiency, given the output voltage V_{out} and the fire angles of the rectifier MOSFETs $Q_1, \ldots, Q_4$. Let us refer to the time interval $[T_s/2; T_s]$ to define such fire angles. As shown in Figs. 2(b) and 3(b), α is the angle between the zero-crossing current $i_2(t)$ and the falling voltage $v_2(t)$; β is the angle between the rising voltage $v_2(t)$ and the zero-crossing current $i_2(t)$. The relations among D, ϕ, α and β are given by (1):

$$\alpha = \frac{\pi(1-D)}{2} + \phi \;\; ; \;\; \beta = \frac{\pi(1-D)}{2} - \phi \tag{1}$$

The values of α and β of practical interest are those ones ensuring that $0 < D < 1$ and $-\pi/2 < \phi < \pi/2$, for unidirectional operation, or $0 < D < 1$ and $-\pi < \phi < \pi$, for bidirectional operation. In this paper, unidirectional operation only is considered. If $f_s = 1/T_s$ is the operation frequency of the primary side inverter, $v_1(t)$, $v_2(t)$, $i_1(t)$ and $i_2(t)$ can be approximated to be pure sinusoids and written as the sum of cosine terms, by applying the first harmonic solution of the WPTS:

$$v_1(t) = V_1 \cos(\omega_s t + \varphi_{V_1}) \;\; ; \;\; i_1(t) = I_1 \cos(\omega_s t + \varphi_{I_1}) \tag{2.a}$$

$$v_2(t) = V_2 \cos(\omega_s t + \varphi_{V_2}) \;\; ; \;\; i_2(t) = I_2 \cos(\omega_s t + \varphi_{I_2}) \tag{2.b}$$

Therefore, the equations of the WPTS transmitter–receiver coupled loops can be derived as:

$$\overline{V}_1 = \dot{Z}_1 \overline{I}_1 - j\omega_s M \overline{I}_2 \tag{3.a}$$

$$\overline{V}_2 + \dot{Z}_2 \overline{I}_2 = j\omega_s M \overline{I}_1 \tag{3.b}$$

where

$$\overline{V}_1 = V_1 e^{j\phi_{V_1}}, \quad \overline{I}_1 = I_1 e^{j\phi_{I_1}}, \quad \overline{V}_2 = V_2 e^{j\phi_{V_2}}, \quad \overline{I_2} = I_2 e^{j\phi_{I_2}} \tag{4.a}$$

$$\dot{Z}_1 = R_{L_1} + R_{s_1} + 2R_{dson,inv} + j\omega_s L_1 + (j\omega_s C_{s1})^{-1} = Z_1 e^{j\phi_{Z_1}} \tag{4.b}$$

$$\dot{Z}_2 = R_{L_2} + R_{s_2} + 2R_{dson,rec} + j\omega_s L_2 + (j\omega_s C_{s2})^{-1} = Z_2 e^{j\phi_{Z_2}} \tag{4.c}$$

Merging (3) and (4) yields to the equations system (5.a) and (5.b), in which the real part and the imaginary part have been separated each other and put equal to zero:

$$\Gamma_{im} = \omega_s M V_1 \sin\left(\phi_{V_1} + \frac{\pi}{2}\right) - Z_1 Z_2 I_2 \sin(\phi_{Z_1} + \phi_{Z_2} + \phi_{I_2}) - \omega_s^2 M^2 I_2 \sin(\phi_{I_2}) - V_2 Z_1 \sin(\phi_{V_2} + j\phi_{Z_1}) = 0 \tag{5.a}$$

$$\Gamma_{re} = \omega_s M V_1 \cos\left(\phi_{V_1} + \frac{\pi}{2}\right) - Z_1 Z_2 I_2 \cos(\phi_{Z_1} + \phi_{Z_2} + \phi_{I_2}) - \omega_s^2 M^2 I_2 \cos(\phi_{I_2}) - V_2 Z_1 \cos(\phi_{V_2} + j\phi_{Z_1}) = 0 \tag{5.b}$$

From Fourier formulas, the transmitter voltage V_1 and the receiver voltages V_2 are given by (6):

$$V_1 = \frac{4}{\pi} V_{in} \quad ; \quad V_2 = \frac{2}{\pi} V_{out} \sqrt{2(c_\alpha c_\beta - s_\alpha s_\beta)} \tag{6}$$

Let us also assume the instant where the secondary side current $i_2(t)$ crosses zero with positive derivative as a reference for the phase angles, and in particular $\phi_{I2} = -\pi/2$. The resulting phase for the voltage V_2 is given by (7):

$$\phi_{V_2} = \phi_{I_2} - \frac{1}{2}(\alpha - \beta) = -\frac{1}{2}(\pi - \alpha + \beta) \tag{7}$$

Therefore, the quantities Z_1, Z_2, V_1, M, ω_s, ϕ_{Z1}, ϕ_{Z2}, ϕ_{I2} are all known, whereas V_2 and ϕ_{V2} are depending on the values of α, β and $V_{out} = V_{bat} + R_{bat}\ I_{out}$. Neglecting the rectifier switching losses as first approximation, the output current I_{out} represents the average output current of the rectifier, which is related to the current I_2 as in (8):

$$I_{out} \simeq I_{rect,av} = \frac{1}{T_s} \int_{\alpha}^{\pi-\beta} I_2 \sin(\vartheta) d\vartheta = I_2 \frac{c_\alpha + c_\beta}{\pi} \tag{8}$$

Therefore, given V_{in}, V_{bat} and R_{bat}, the remaining unknowns I_2 and ϕ_{V1} can determined by solving the equations system (5) for different couples of values α and β (or equivalently, of duty D and phase ϕ). This non-linear system (5) has never been solved in literature. All previous studies [20,27] are based on approximations that allow to achieve an estimation of the current I_{out}. In order to prevent uncertainties in the calculation of losses caused by simplified approximations applied in previous studies, in this paper a Newton–Raphson algorithm [28] is adopted to solve the equations system (5). The Newton–Raphson is one of the most widely used methods for root finding, since it is a powerful technique for numerically solving non-linear equations. Some additional details on the Newton–Raphson method and its practical implementation, as well as on other methods for root finding, can be found in [29]. Starting from guess values $\overline{X}_0 = [I_2^{(0)}, \phi_{V_1}^{(0)}]^T$, the matrix Eq. (9)

$$\overline{X}_{n+1} = \overline{X}_n - \left[\mathbf{J}_\Gamma(\overline{X}_n)\right]^{-1} \overline{\Gamma}_n(\overline{X}_n) \quad \text{for } n = 0, 1, \ldots, N_{end} \tag{9}$$

is iterated until $\|\overline{\Gamma}_{n+1}(\overline{X}_{n+1}) - \overline{\Gamma}_n(\overline{X}_n)\| < \varepsilon$, where ε is the required tolerance and:

$$\overline{X}_n = [I_2^{(n)}, \phi_{V_1}^{(n)}]^T \quad \overline{\Gamma}_n(\overline{X}_n) = [\Gamma_{re}(\overline{X}_n), \Gamma_{im}(\overline{X}_n)]^T \tag{10.a}$$

$$\mathbf{J}_\Gamma(\overline{X}_n) = \begin{bmatrix} \frac{\partial \Gamma_{re}}{\partial I_2}\Big|_{\overline{X}_n} & \frac{\partial \Gamma_{re}}{\partial \phi_{V_1}}\Big|_{\overline{X}_n} \\ \frac{\partial \Gamma_{im}}{\partial I_2}\Big|_{\overline{X}_n} & \frac{\partial \Gamma_{im}}{\partial \phi_{V_1}}\Big|_{\overline{X}_n} \end{bmatrix} \tag{10.b}$$

Table 2
Rectifier losses.

Conduction losses	$P_{cond,rec} = 2R_{dson,rec} I_{2,rms}^2$
Body diode losses at $i_2 = I_2 s_\alpha$ and $i_2 = I_2\ s_\beta$	$P_{body,rec} = 2V_{sd,rec} I_2 (\lvert s_\alpha \rvert + \lvert s_\beta \rvert) t_{dt,rec} f_s$
Gate losses of Q_1, Q_2, Q_3, Q_4	$P_{gate,rec} = 4Q_{g,rec} V_{dr,rec} f_s$
For $\alpha > 0$; $\beta > 0$: Q_2, Q_4 turn OFF losses at $i_2 = I_2 s_\alpha$ Q_1, Q_3 turn ON losses at $i_2 = I_2 s_\beta$	$P_{on-off,rec} = V_{out} f_s [I_2 s_\alpha t_{off\alpha,rec} + I_2 s_\beta t_{on\beta,rec} + C_{oss,rec} V_{out} + 2Q_{rr,rec}]$ $t_{off\alpha,rec} = \frac{Q_{gsw,rec} R_{goff,rec}}{V_{th,rec} + \frac{I_2 s_\alpha}{g_{fs,rec}}}$ $t_{on\beta,rec} = \frac{Q_{gsw,rec} R_{gon,rec}}{V_{dr,rec} - V_{th,rec} - \frac{I_2 s_\beta}{g_{fs,rec}}}$
For $\alpha > 0$; $\beta < 0$: Q_2, Q_4 turn OFF losses at $i_2 = I_2 s_\alpha$ Q_1, Q_3 turn OFF losses at $i_2 = -I_2 s_\beta$ ($s_\beta < 0$)	$P_{on-off,rec} = V_{out} f_s [I_2 s_\alpha t_{off\alpha,rec} - I_2 s_\beta t_{off\beta,rec}]$ $t_{off\alpha,rec} = \frac{Q_{gsw,rec} R_{goff,rec}}{V_{th,rec} + \frac{I_2 s_\alpha}{g_{fs,rec}}}$ $t_{off\beta,rec} = \frac{Q_{gsw,rec} R_{goff,rec}}{V_{th,rec} - \frac{I_2 s_\beta}{g_{fs,rec}}}$
For $\alpha < 0$; $\beta > 0$: Q_2, Q_4 turn ON losses at $i_2 = I_2 s_\beta$ Q_1, Q_3 turn ON losses at $i_2 = -I_2 s_\alpha$ ($s_\alpha < 0$)	$P_{on-off,rec} = V_{out} f_s [-I_2 s_\alpha t_{on\alpha,rec} + I_2 s_\beta t_{on\beta,rec} + 2C_{oss,rec} V_{out} + 4Q_{rr,rec}]$ $t_{on\alpha,rec} = \frac{Q_{gsw,rec} R_{gon,rec}}{V_{dr,rec} - V_{th,rec} + \frac{I_2 s_\alpha}{g_{fs,rec}}}$ $t_{on\beta,rec} = \frac{Q_{gsw,rec} R_{gon,rec}}{V_{dr,rec} - V_{th,rec} - \frac{I_2 s_\beta}{g_{fs,rec}}}$

Table 3
Inverter losses.

Conduction losses	$P_{cond,inv} = 2R_{dson,inv} I_{1,rms}^2$
Body diode losses at $i_1 = I_1 s_\phi$	$P_{body,inv} = 4V_{sd,inv} I_1 s_\phi t_{dt,inv} f_s$
Gate losses of M_1, M_2, M_3, M_4	$P_{gate,inv} = 4Q_{g,inv} V_{dr,inv} f_s$
$\phi < 0$: M_1, M_2, M_3, M_4 turn OFF losses at $i_1 = I_1 s_\phi$	$P_{on-off,inv} = 2V_s I_1 s_\phi t_{off,inv} f_s$ $t_{off,inv} = \frac{Q_{gsw,inv} R_{goff,inv}}{V_{th,inv} + \frac{I_1 s_\phi}{g_{fs,inv}}}$
$\phi > 0$[a]: M_1, M_2, M_3, M_4 turn ON losses at $i_1 = I_1 s_\phi$	$P_{on-off,inv} = 2V_s [I_1 s_\phi t_{on,inv} + C_{oss,inv} V_s + 2Q_{rr,inv}] f_s$ $t_{on,inv} = \frac{Q_{gsw,inv} R_{gon,inv}}{V_{dr,inv} - V_{th,inv} - \frac{I_1 s_\phi}{g_{fs,inv}}}$

[a] When the capacitance of transmitter and receiver capacitors is de-rated with respect to the nominal resonant value, the current $i_1(t)$ can lead the voltage $v_1(t)$.

The key point is to understand what is the net output current I_{out} getting off the WPTS. The solution of the matrix Eq. (9) takes into account the ohmic losses of the entire WPTS, including the effect of inverter and rectifier MOSFET parasitic resistances, as highlighted in the expressions of impedances $\dot{Z}_1$ and $\dot{Z}_2$, given in (4.b) and (4.c), respectively. Eq. (8) yields an overestimation of the power that the WPTS can deliver at given α, β and input and load operating conditions. In reality, part of the output current I_{out} is lost because of the rectifier MOSFETs switching losses. The relationship between the current I_2 and the net average output current $I_{out,net}$ of the WPTS rectifier is given by Eq. (11):

$$I_{out,net} = I_{rect,av} - I_{sw,rec} \tag{11}$$

The current $I_{sw,rec}$ can be considered as sought by an equivalent dissipative current source connected in parallel to the rectifier output of Fig. 1. Such current effectively allows analyzing the impact of rectifier switching losses on the output power and efficiency of the WPTS. The technical literature is rich of papers discussing MOSFETs switching losses, from physical level [30] to behavioral level [31,32]. Accordingly, the global rectifier losses can be summarized as shown in the loss formulae of Table 2, obtained by means of models discussed in [32] (the reader can refer to Table 1 for details about all parameters). Based on these formulae, the equivalent current $I_{sw,rec}$ is given by (12):

$$\begin{aligned} I_{sw,rec} &= \frac{P_{on-off,rec} + P_{gate,rec} + P_{body,rec}}{V_{out}} \\ &= \frac{P_{on-off,rec} + P_{gate,rec} + P_{body,rec}}{V_{bat} + R_{bat} I_{out,net}} \end{aligned} \tag{12}$$

Since $I_{out,net}$ depends on $I_{sw,rec}$, and in turn $I_{sw,rec}$ depends on the output load current and voltage, Eqs. (11) and (12) require to be iteratively solved, until a convergent result is eventually achieved for $I_{sw,rec}$. In particular, from (12) the net average output current $I_{out,net}$ can be rewritten as shown in (13):

$$I_{out,net} = I_2 \frac{c_\alpha + c_\beta}{\pi} - I_{sw,rec} = I_2 \frac{c_\alpha + c_\beta}{\pi} - f_s \Lambda(I_2, \alpha, \beta) \tag{13}$$

where

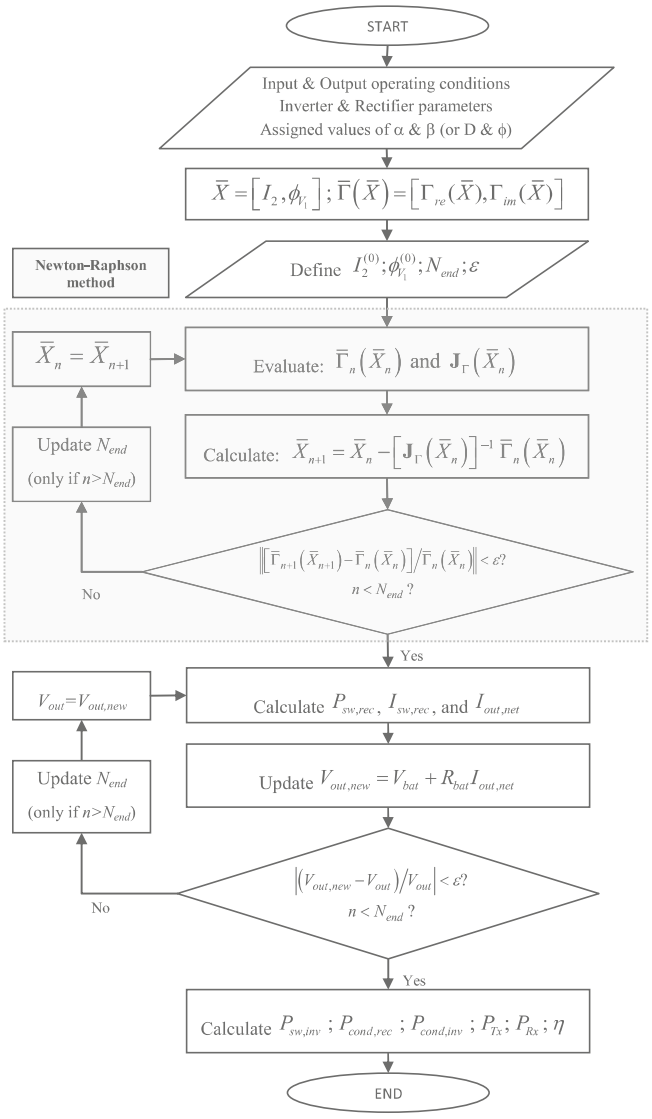

Fig. 4. Loss analysis model flowchart.

$$\Lambda(I_2, \alpha, \beta) = \begin{cases} 2\frac{V_{sd,rec}}{V_{out}} I_2 (|s_\alpha| + |s_\beta|) t_{dt,rec} + \frac{I_2 s_\alpha Q_{gsw,rec} R_{goff,rec}}{V_{th,rec} + \frac{I_2 s_\alpha}{g_{fs,rec}}} + \frac{I_2 s_\beta Q_{gsw,rec} R_{gon,rec}}{V_{dr,rec} - V_{th,rec} - \frac{I_2 s_\beta}{g_{fs,rec}}} + C_{oss,rec} V_{out} + 2Q_{rr,rec} + 4Q_{g,rec} \frac{V_{dr,rec}}{V_{out}} & \{\alpha > 0, \beta > 0 \\ 2\frac{V_{sd,rec}}{V_{out}} I_2 (|s_\alpha| + |s_\beta|) t_{dt,rec} + \frac{I_2 s_\alpha Q_{gsw,rec} R_{goff,rec}}{V_{th,rec} + \frac{I_2 s_\alpha}{g_{fs,rec}}} - \frac{I_2 s_\beta Q_{gsw,rec} R_{goff,rec}}{V_{th,rec} - \frac{I_2 s_\beta}{g_{fs,rec}}} + 4Q_{g,rec} \frac{V_{dr,rec}}{V_{out}} & \{\alpha > 0, \beta < 0 \\ 2\frac{V_{sd,rec}}{V_{out}} I_2 (|s_\alpha| + |s_\beta|) t_{dt,rec} - \frac{I_2 s_\alpha Q_{gsw,rec} R_{gon,rec}}{V_{dr,rec} - V_{th,rec} + \frac{I_2 s_\alpha}{g_{fs,rec}}} + \frac{I_2 s_\beta Q_{gsw,rec} R_{gon,rec}}{V_{dr,rec} - V_{th,rec} - \frac{I_2 s_\beta}{g_{fs,rec}}} + 2C_{oss,rec} V_{out} + 4Q_{rr,rec} + 4Q_{g,rec} \frac{V_{dr,rec}}{V_{out}} & \{\alpha < 0, \beta > 0 \end{cases}$$
$$V_{out} = V_{bat} + R_{bat} \left(I_2 \frac{c_\alpha + c_\beta}{\pi} \right) \tag{14}$$

Eq. (13) highlights that the net output current $I_{out,net}$, accounting for the effect of the rectifier MOSFET losses, is correlated to the current I_2 by a heavily non-linear equation, which is also dependant on the sign of fire angles α and β. Solving the equations system (9), the current I_2 is eventually known, and the phasor $\bar{I}_1$ of transmitter loop current can be determined by means of Eq. (15):

$$\bar{I}_1 = \frac{\bar{V}_1 + j\omega_s M \bar{I}_2}{\dot{Z}_1} \tag{15}$$

Eq. (15) provides the elements to calculate the inverter losses, which are summarized in Table 3. The effect of the inverter switching losses $P_{sw,inv}$ can be modeled by means of an equivalent current source in parallel to the inverter input, whose current is given by (16):

$$I_{sw,inv} = \frac{P_{on-off,inv} + P_{gate,inv} + P_{body,inv}}{V_{in}} \tag{16}$$

The transmitter and receiver conduction losses can be calculated by means of Eq. (17):

$$P_{Tx} = (R_{C_1} + R_{L_1})I_{1,rms}^2 \;\; ; \;\; P_{Rx} = (R_{c_2} + R_{L_2})I_{2,rms}^2 \tag{17}$$

The overall WPTS efficiency is then given by

$$\eta = \frac{P_{out}}{P_{out} + P_{inv} + P_{Tx} + P_{Rx} + P_{rec}} = \frac{V_{out}I_{out,net}}{V_{out}I_{out,net} + (P_{cond,inv} + P_{sw,inv}) + P_{Tx} + P_{Rx} + (P_{cond,rec} + P_{sw,rec})} \tag{18}$$

The method of proposed analysis has been summarized in the flowchart of Fig. 4 and it can be used to make a comparative analysis of the impact of different MOSFETs in the output power and efficiency of a WPTS, given a certain setup of the transmitter and receiver coils.

Loss analysis and experimental verification

The WPTS adopted for the application of the loss analysis method and the validation of the model presented in section 'WPTS modeling' is characterized by the following nominal operating parameters: $f_s = 6.78$ MHz, $L_1 = 7.5$ μH, $Q_{L1} = 150$, $L_2 = 0.93$ μH, $Q_{L2} = 40$, $Q_{C1} = 1000$, $Q_{C2} = 1000$, $C_{1s} = 1/(\omega_s^2 L_1) = 73.5$ pF, $C_{2s} = 1/(\omega_s^2 L_2) = 593$ pF. The WPTS is realized physically with transmitter and the receiver coils shown in Fig. 5(a), whose characteristics are summarized in Table 4. The design and optimization of the coils is herein not discussed, as it goes beyond the subject of the paper. The goal, in fact, is to investigate the impact of MOSFET losses on the WPTS output power and efficiency, for given transmitter and receiver coils characteristics. Placing the receiver coil in various positions with respect to the transmitter coil yields different values of the coupling factor. The center position (hereinafter, referred to the "ce" suffix) of Fig. 5(b) and the corner position ("co" suffix) of Fig. 5(c), with 6 mm or 9 mm vertical distance among coils, correspond to values of coupling factors $K_{ce,6} = 0.076$, $K_{ce,9} = 0.069$, $K_{co,9} = 0.067$, calculated by means of ANSYS® High Frequency Structural Simulator (HFSS), an industry standard software for simulating 3-D electromagnetic fields [33].

The ROHM RUF015N02 MOSFET and Texas Instruments LM5113-5A gate driver providing a gate voltage $V_{dr} = 5$V and a dead-time $t_{dt} = 2$ ns have been used for the rectifier and inverter implementation. The main parameters of RUF015N02 MOSFETs are summarized in Table 5. Two Xilinx Spartan-6 FPGA have been also used for the inverter and rectifier control implementation.

Fig. 6 shows the measurement setup adopted for the experimental tests, comprised of a Tektronix DPO 4054 Oscilloscope, a Tektronix TCP 312 30A current probe with Tektronix TCP A300 amplifier, a Tektronix TCP0030 current probe, two Tektronix TDP1000 differential voltage probes, an Agilent E3631A power supply, four HP34401A multi-meters and a Chroma 63100-5 electronic load with 63610-80-20 modules.

Table 4
WPTS: coils specifications.

Tx coils		Rx coils	
Diameter	70 × 70 mm²	Diameter	15 × 15 mm²
Trace width	1 mm	Trace width	0.3 mm
Turns	9	Turns	8
Spacing between turns	1 mm	Spacing between turns	0.3 mm
Inductance L_1	7.5 μH	Inductance L_2	0.93 μH
Q_{L1} (@6.78 MHz)	150	Q_{L2} (@6.78 MHz)	40

Table 5
ROHM RUF015N02 parameters.

RUF015N02: main parameter			
V_{th} [V]	0.3	V_{sd} [V]	1.2
g_{fs} [S]	1.6	Q_{rr} [nC]	0.1
C_{oss} [pF]	18	R_g [Ω]	4
Q_g [nC]	1.8	$R_{gd,on}$ [Ω]	14
Q_{gs} [nC]	0.3	$R_{gd,off}$ [Ω]	1
Q_{gd} [nC]	0.3	$R_{dson} + R_{sns}$ [mΩ]	255

Before the execution of experimental test, a preliminary measurement of capacitances Cs_1 and Cs_2 has been realized, and a mismatch of about 1% and 2.5% has been measured for the capacitances Cs_1 and Cs_2 with respect to nominal capacitance values $Cs_{1,nom} = 1/(\omega_s^2 L_1)$ and $Cs_{2,nom} = 1/(\omega_s^2 L_2)$. The maps of Fig. 7 show the results of experimental measurements of the WPTS output power and efficiency, executed over the duty-cycle range $D \in [0.2; 1]$ and the phase range $\phi/\pi \in [-0.4; 0.4]$, for $V_{in} = 8$ V, $V_{bat} = 5.3$ V and $R_{bat} = 1\,\Omega$. Three case studies, corresponding to the following operating conditions:

$$\text{(A)}: \; D = 1 \;\&\; \phi/\pi = 0$$
$$\text{(B)}: \; D = 0.68 \;\&\; \phi/\pi = 0.19$$
$$\text{(C)}: \; D = 0.52 \;\&\; \phi/\pi = -0.29$$

have been selected to show the different impact of switching losses depending on the type of commutation of MOSFETs. The experimental measurements of TX coil and RX coil voltages and currents are shown in Fig. 8 for each case study. Fig. 8(a) shows the case (A), where the current and voltage waveforms are almost perfectly in phase ($\phi \cong 0$) and the duty-cycle of the voltage square-wave is almost 100%. In Fig. 8(b) and (c), corresponding to case (B) and case (C), a phase lead condition ($\phi > 0$) and a phase lag condition ($\phi < 0$) is observed, respectively.

The non linear model (5) and the Newton–Raphson algorithm (9) and (10) illustrated in section 'WPTS modeling' have been implemented in MATLAB, to analyze the WPTS output power, the

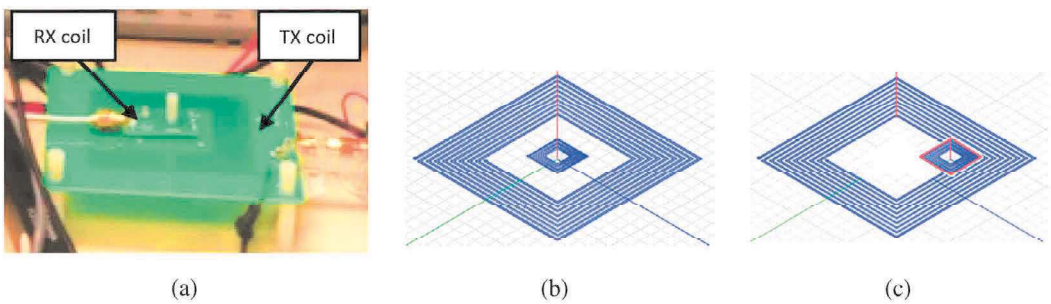

Fig. 5. (a) WPTS coils and relative positions adopted in the experimental measurements, (b) center position and (c) corner position.

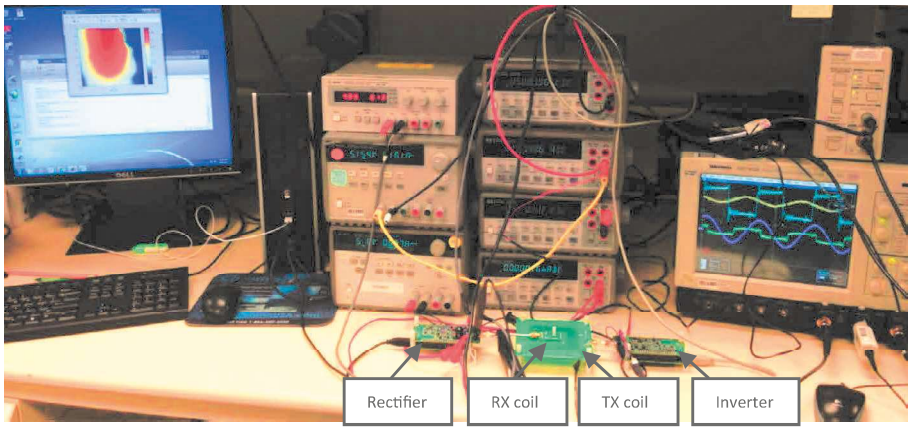

Fig. 6. WPTS and experimental measurement set-up.

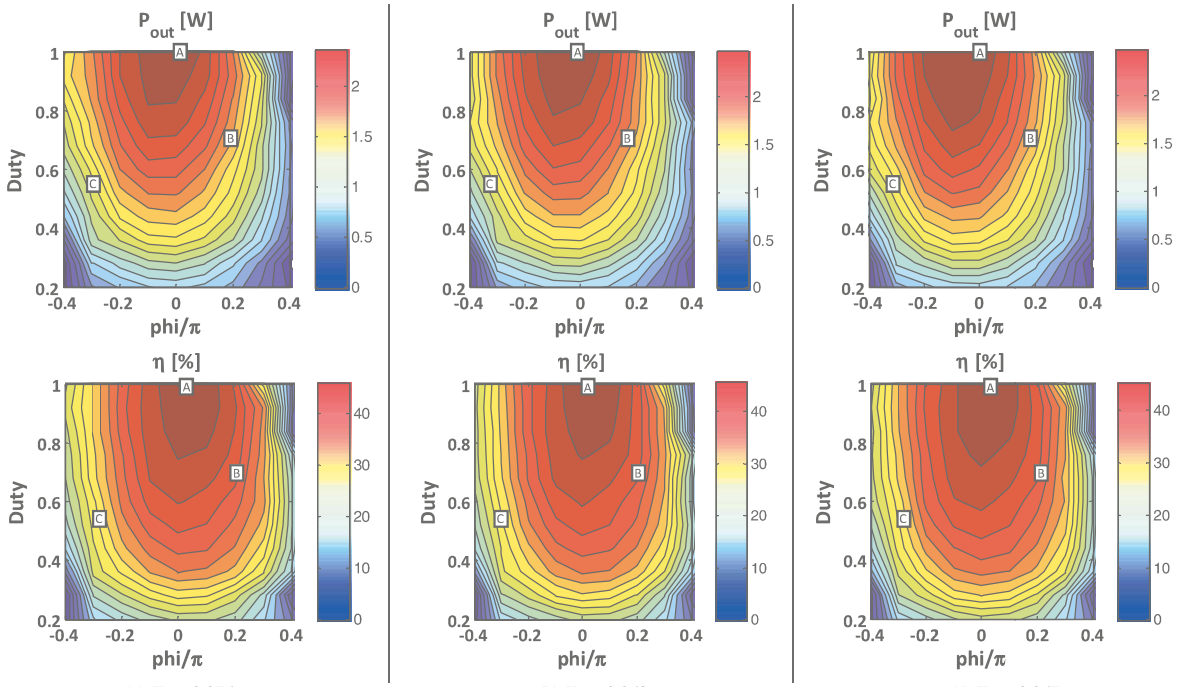

(a) $K_{ce,6}$=0.076 (b) $K_{ce,9}$=0.069 (c) $K_{co,9}$=0.067

Fig. 7. Experimental measurements of output power (top) and efficiency (bottom): RX coil at 6 mm distance and centered position (a), RX coil at 9 mm distance and centered position (b), RX coil at 9 mm distance and corner position (c).

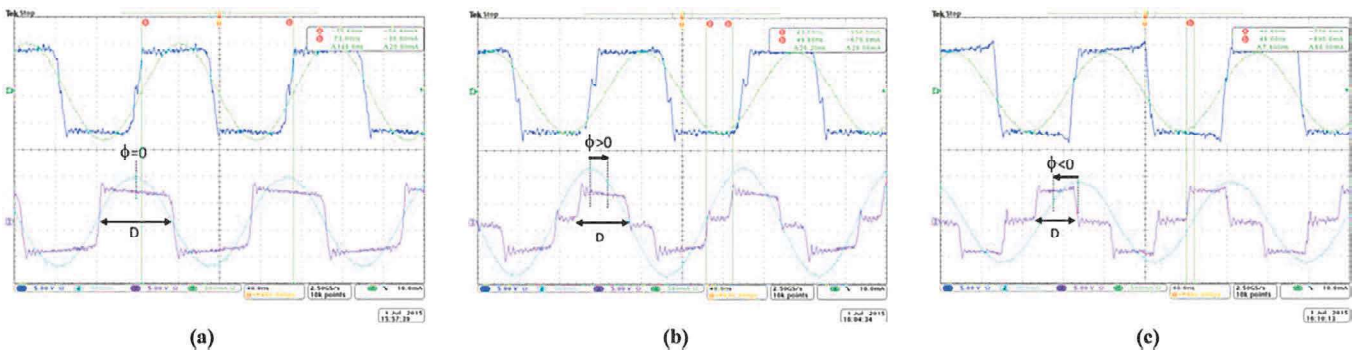

(a) (b) (c)

Fig. 8. Oscilloscope screenshots for: $D = 1$, $\phi/\pi = 0$ (a); $D = 0.68$, $\phi/\pi = 0.2$ (b); $D = 0.52$, $\phi/\pi = -0.3$ (c). Blue trace (CH1: 5 V/div): Tx bridge differential output voltage; Green trace (CH2: 500 mA/div): Tx coil current; magenta trace (CH3: 5 V/div): Rx bridge differential input voltage; Turquoise trace (CH4: 500 mA/div): Rx coil current. (For interpretation of the references to color in this figure legend, the reader is referred to the web version of this article.)

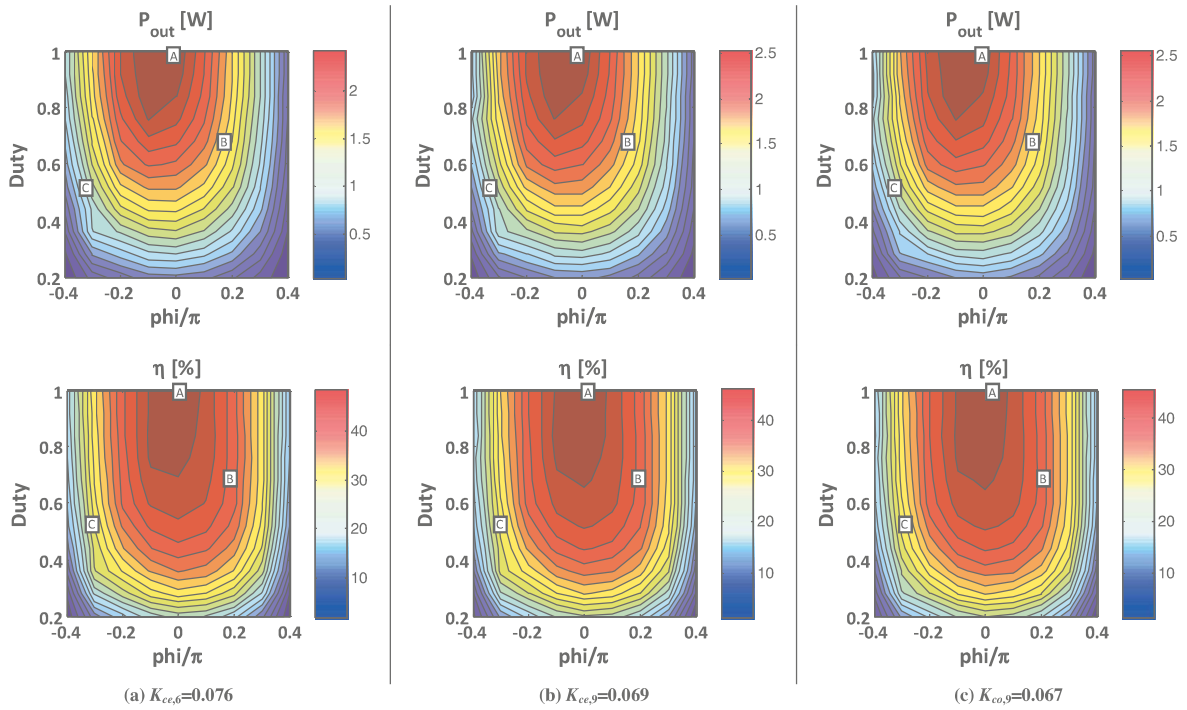

(a) $K_{ce,6}$=0.076 (b) $K_{ce,9}$=0.069 (c) $K_{co,9}$=0.067

Fig. 9. MATLAB simulated results of output power (top) and efficiency (bottom): RX coil at 6 mm distance and centered position (a), RX coil at 9 mm distance and centered position (b), RX coil at 9 mm distance and corner position (c).

efficiency and the overall losses, in the same conditions of the experimental tests. The simulated maps given in Fig. 9, compared to the experimental maps of Fig. 7, show that the predictions of the proposed model are correct over the entire range of investigation.

MOSFETs impact on WPTS output power and efficiency

The maps of Fig. 10 provide the detail of coils losses and of conduction and switching losses of the inverter and rectifier. The maps highlight that the MOSFETs switching losses are strongly varying with the $\{D, \phi\}$ operating conditions and that they are comparable or even exceeding the conduction losses. The switching losses have indeed a big impact on the global performance of the WPTS. In order to better emphasize such impact, the WPTS has been analyzed by means of the proposed model without switching losses. The resulting power and efficiency maps are shown in Fig. 11.

The measured *vs* predicted output power and global efficiency for the three case studies (namely, $K_{ce,6}$, $K_{ce,9}$ and $K_{co,9}$) and three main operating conditions (namely, case (A), case (B) and case

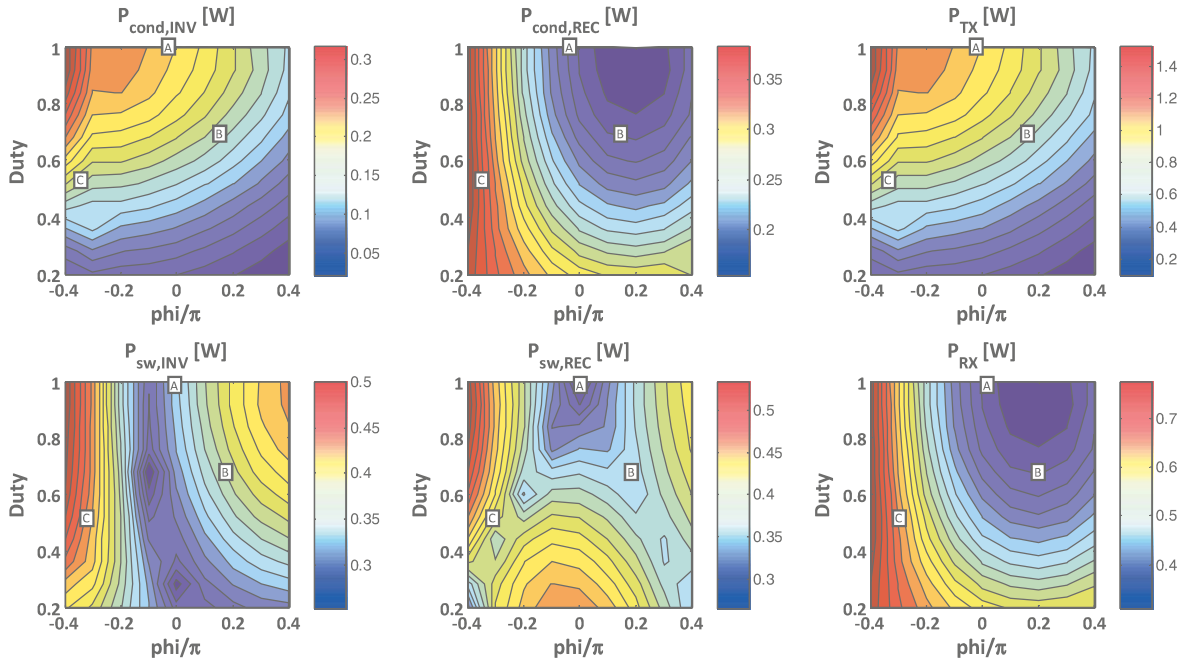

Fig. 10. MATLAB simulated results for RX coil at 6 mm distance and centered position ($K_{ce,6}$ = 0.076).

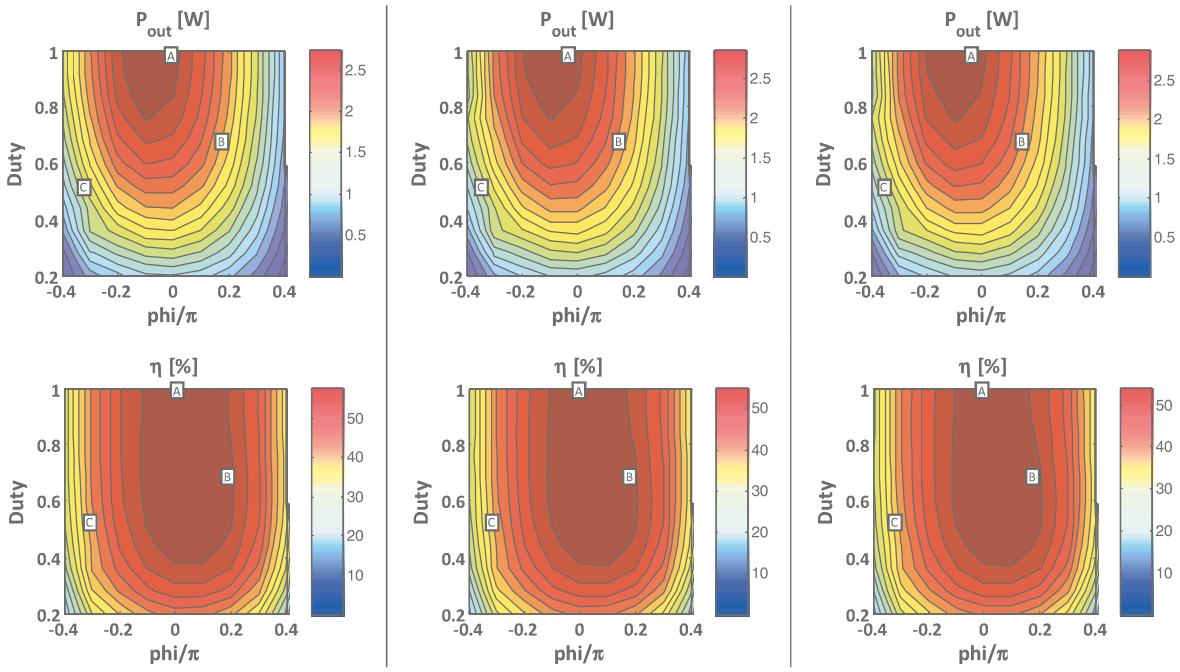

(a) $K_{ce,6}$=0.076 (b) $K_{ce,9}$=0.069 (c) $K_{co,9}$=0.067

Fig. 11. MATLAB simulated results of output power (top) and efficiency (bottom) without switching losses evaluation: RX coil at 6 mm distance and centered position (a), RX coil at 9 mm distance and centered position (b), RX coil at 9 mm distance and corner position (c).

Table 6
Experimental (EXP.) and MATLAB simulated (MAT.) output power and efficiency values for K_{ce6}, K_{ce9}, K_{co9}.

Case study	Losses ref.	P_{out} [W]									η [%]								
		case A			*case B*			*case C*			*case A*			*case B*			*case C*		
		EXP.	MAT.	ε%	EXP.	MAT.	ε%	EXP.	MAT.	ε%	EXP.	MAT.	ε%	EXP.	MAT.	ε%	EXP.	MAT.	ε%
$K_{ce,6}$ = 0.076	With SW losses	2.47	2.53	2.4	1.72	1.58	−8.1	1.32	1.20	−9.1	48.4	50.8	5.0	42.3	42.5	0.5	28.6	30.0	4.9
	W/o SW losses		2.80	13.3		1.95	13.3		1.62	22.8		60.2	24.4		58.4	38.0		45.4	58.9
$K_{ce,9}$ = 0.069	With SW losses	2.61	2.63	0.8	1.80	1.67	−7.2	1.48	1.32	−10.8	47.9	48.4	1.0	41.4	41.0	−1.0	29.0	29.0	0.0
	W/o SW losses		2.90	11.1		2.04	13.4		1.75	18.3		57.0	18.9		55.5	34.0		42.6	46.7
$K_{co,9}$ = 0.067	With SW losses	2.59	2.65	2.3	1.78	1.69	−5.1	1.55	1.36	−12.3	47.6	47.7	0.2	41.1	40.5	−1.5	29.4	28.7	−2.4
	W/o SW losses		2.93	13.0		2.07	16.1		1.79	15.5		55.9	17.5		54.5	32.7		41.7	41.7

(C)), with and without switching losses, are all summarized in Table 6. Fig. 12 shows a graphical summary of such results, mostly highlighting the high level of efficiency accuracy of the proposed modeling.

The MOSFET parameters adopted to obtain the MATLAB simulation results summarized in Table 6 are the same available in the manufacturers' datasheet, referred to 25 °C junction temperature. This is the origin of the different sign and magnitude of the error in higher power (case (A)) *vs* lower power (cases (B) and (C)) operating conditions. Some manufacturers provide all the data relevant to thermal properties of MOSFETs, namely the dependency of channel resistance R_{dson}, trans-conductance g_{fs} and gate-source voltage threshold V_{th} *vs* the junction temperature. In this case, the power and efficiency analysis can be refined, to further improve the accuracy of the simulation results, by including an additional thermal loop in the solution of the proposed model. Comparing the maps of Figs. 9 and 11 and the data of Table 6 highlights that the predictions obtained by neglecting the switching losses are affected by a big error, with a big overestimation of the WPTS power and efficiency. Using MOSFETs with reduced switching losses is an obvious recommendation for a high-frequency application like the one under investigation. However, MOSFETs ensuring lower switching losses are characterized by smaller capacitances and gate charge values *vs* higher channel resistance values. Therefore, a trade-off is needed to optimize the power and efficiency performance of a high-frequency WPTS.

The method proposed in this paper can be effectively used to optimize the 2 W@6.78 MHz WPTS by finding the most appropriate MOSFETs for this application. Table 7 shows the results of a comparative loss and efficiency analysis among six devices (five MOSFET and one GaN transistor) characterized by voltage and current ratings suitable for the application. These results take into account the switching losses for all the devices and show that the RUF015N02 and NTJS4405N MOSFETs provide very good performances among the traditional MOSFETs technology. However, the enhancement GaN transistors confirm their best performances working in this low-power high-frequency application.

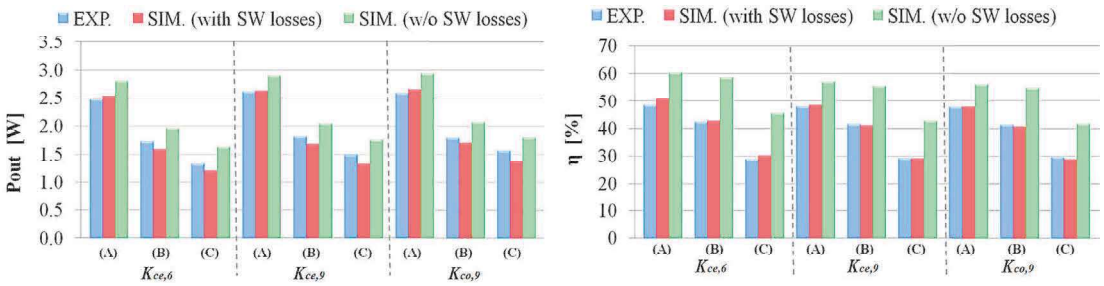

Fig. 12. Experimental and simulated output power (left) and efficiency (right) for K_{ce6}, K_{ce9}, K_{co9}, with and w/o switching losses.

Table 7
Simulated output power and efficiency (for $K_{ce,6} = 0.076$).

Parts (manufacturer)	Ratings	P_{out} [W]			η [%]		
		Case A	Case B	Case C	Case A	Case B	Case C
FDN327N (FAIRCHILD)	20 V, 2.0 A	2.31	0.94	0.64	42.0	22.1	13.4
RTQ020N03 (ROHM)	30 V, 2.0 A	2.56	1.48	1.04	49.4	37.8	24.9
RUF015N02 (ROHM)	20 V, 1.5 A	2.53	1.58	1.20	50.8	42.5	30.0
RSF014N03 (ROHM)	30 V, 1.4 A	2.42	1.58	1.15	47.9	41.0	28.3
NTJS4405N (ON SEMI)	25 V, 1.2 A	2.50	1.69	1.27	50.7	45.6	32.3
EPC2040[a] (EPC)	15 V, 3.4 A	2.77	1.86	1.48	57.9	53.6	41.9

The results presented above confirm that the design of WPTS for low-power high-frequency applications, such as portable and wearable devices, requires a complete loss modeling, including the switching losses of devices in the inverter and rectifier conversion stages. A correct loss mapping has an important impact beyond the MOSFETs selection. In fact, by observing the power and efficiency maps of Figs. 9 and 10, it can be noticed that there are infinite couples of values $\{D, \phi\}$ providing a certain output power at different levels of efficiency and with different losses distribution among the primary and the secondary sides of the WPTS. The maps of inverter, rectifier, TX and RX coils loss shown in Fig. 10 also highlight the asymmetry and duality of inverter *vs* rectifier loss determined by D and ϕ. Thus, there can be control design solutions providing the minimization of receiver and rectifier losses for a given power *vs* efficiency trade-off, that is a challenging goal for wearable devices wireless charging.

Conclusions

The model proposed in this paper for the loss analysis of low power high-frequency Wireless Power Transfer Systems (WPTSs) allows to investigate the influence of semiconductor devices parameters on the overall WPTS performance. The proposed WPTS modeling may include switching losses of semiconductor devices, parameters mismatch of resonant elements, as well as modulation of duty-cycle and phase of secondary side rectifier. The experimental measurements realized on a 2 W@6.78 MHz WPTS presented in the paper demonstrate the validity of the analysis. The results highlight the possibility to identify optimal combinations of WPTS elements, power MOSFETs and operating conditions, providing the best trade-off among the desired output power, the loss distribution among the primary and the secondary sides of the WPTS and the global system efficiency.

Acknowledgements

This research has been supported by Texas Instruments Inc., USA, through the project "Wireless charging Parameterized Model and Design" (300394CES14FEMIA), and by the University of Salerno, Italy, through the projects "Wireless Power Transfer Systems" (300394FRB14FEMIA and 300394FRB15FEMIA).

References

[1] Hui SYR, Zhong W, Lee CK. A critical review of recent progress in mid-range wireless power transfer. IEEE Trans Power Electron 2014;29(9).
[2] Jang Y, Jovanovic MM. A contactless electrical energy transmission system for portable-telephone battery chargers. IEEE Trans Industr Electron 2003;50(3).
[3] Liu X, Hui SYR. Optimal design of a hybrid winding structure for planar contactless battery charging platform. IEEE Trans Power Electron 2008;23(1).
[4] Li S, Mi CC. Wireless power transfer for electric vehicle applications. IEEE J Emerg Select Topics n Power Electron 2015;3(1).
[5] Zheng C, Lai JS, Chen R, Faraci WE, Zahid ZU, Gu B, et al. High-efficiency contactless power transfer system for electric vehicle battery charging application. IEEE Trans Power Electron 2008;23(1).
[6] Choi S, Huh J, Lee WY, Lee SW, Rim CT. New cross-segmented power supply rails for roadway-powered electric vehicles. IEEE Trans Power Electron 2013;28(12).
[7] Chen L, Boys JT, Covic GA. Power management for multiple-pickup IPT systems in materials handling applications. IEEE J Emerg Select Topics Power Electron 2015;3(1).
[8] Elliott GAJ, Covic GA, Kacprzak D, Boys JT. A new concept: asymmetrical pick-ups for inductively coupled power transfer monorail systems. IEEE Trans Magn 2006;42(10).
[9] Shiba K, Morimasa A, Hirano H. Design and development of low-loss transformer for powering small implantable medical devices. IEEE Trans Biomed Circ Syst 2010;4(2).
[10] Friedmann J, Groedl F, Kennel R. A novel universal control scheme for transcutaneous energy transfer (TET) applications. IEEE J Emerg Select Topics Power Electron 2015;3(1).
[11] Zhong WX, Zhang C, Liu X, Hui SYR. A methodology for making a three-coil wireless power transfer system more energy efficient than a two-coil counterpart for extended transfer distance. IEEE Trans Power Electron 2015;30(2).
[12] Moon SC, Kim BC, Cho SY, Ahn CH, Moon GW. Analysis and design of a wireless power transfer system with an intermediate coil for high efficiency. IEEE Trans Indust Electron Nov. 2014;61(11).
[13] Hou J, Chen Q, Wong SC, Tse CK, Ruan X. Analysis and control of series/series-parallel compensated resonant converter for contactless power transfer. IEEE J Emerg Select Topics Power Electron 2015;3(1).
[14] Iguchi S, Yeon P, Fuketa H, Ishida K, Sakurai T, Takamiya M. Wireless power transfer with zero-phase-difference capacitance control. IEEE Trans Circ Syst-I: Reg Pap 2015;62(4).
[15] Zhang Y, Zhao Z, Lu T. Quantitative analysis of system efficiency and output power of four-coil resonant wireless power transfer. IEEE J Emerg Select Topics Power Electron 2015;3(1).

[16] Pinuela M, Yates DC, Lucyszyn S, Mitcheson PD. Maximizing DC-to-load efficiency for inductive power transfer. IEEE J Emerg Select Topics Power Electron March 2015;3(1).
[17] Kim Chang-Gyun, Seo Dong-Hyun, You Jung-Sik, Park Jong-Hu, Cho Bo H. Design of a contactless battery charger for cellular phone. IEEE Trans Indust Electron 2001;48(6).
[18] Kim Jinwook, Kim Do-Hyeon, Choi Jeonghee, Kim Kwan-Ho, Park Young-Jin. Free-positioning wireless charging system for small electronic devices using a bowl-shaped transmitting coil. IEEE Trans Microw Theory Tech 2015;63(3).
[19] ITU-R, Radio Regulations, Edition of 2012 <http://www.itu.int/pub/R-REG-RR-2012>.
[20] Berger A, Agostinelli M, Vesti S, Oliver JA, Cobos´JA, Huemer M. A wireless charging system applying phase-shift and amplitude control to maximize efficiency and extractable power. IEEE Trans Power Electron 2015;30(11).
[21] Huwig D, Wambsganss P. Digitally controlled synchronous bridge-rectifier for wireless power receivers. In: 2013 28th Annual IEEE applied power electronics conference and exposition. p. 2598–603.
[22] Pantic Z, Lukic SM. Framework and topology for active tuning of parallel compensated receivers in power transfer systems. IEEE Trans Power Electron 2012;27(11).
[23] Nguyen Bac Xuan, Vilathgamuwa DM, Foo GHB, Wang Peng, Ong A, Madawala UK, Nguyen Trong Duy. An efficiency optimization scheme for bidirectional inductive power transfer systems. IEEE Trans Power Electron Nov. 2015;30 (11):6310–9.
[24] Cai A, Pereira A, Tanzania R, Tan YK, Siek L. A high frequency, high efficiency GaN HFET based inductive power transfer system. In: 2015 IEEE applied power electronics conference and exposition. p. 3094–100.
[25] Florian C, Mastri F, Paganelli RP, Masotti D, Costanzo A. Theoretical and numerical design of a wireless power transmission link with GaN-based transmitter and adaptive receiver. IEEE Trans Microwave Theory Tech 2014;62 (4):931–46.
[26] Chen Q, Jiang L, Hou J, Ren X, Ruan X. Research on bidirectional contactless resonant converter for energy charging between EVs. In: 39th Annual conference of the IEEE industrial electronics society (IECON 2013).
[27] Nguyen BX, Vilathgamuwa DM, Foo GHB, Wang P, Ong A, Madawala UK, et al. An efficiency optimization scheme for bidirectional inductive power transfer systems. IEEE Trans Power Electron 2015;30(11).
[28] Adi Ben-Israel. A Newton–Raphson method for the solution of system of equations. Elsev J Math Anal Appl 1966;15(2).
[29] Press WH, Teukolsky SA, Vetterling WT, Flannery BP. Numerical recipes: the art of scientific computing. 3rd ed. Cambridge University Press; 2007. September.
[30] Aubard L, Verneau G, Crebier JC, Schaeffer C, Avenas Y. Power MOSFET switching waveforms: an empirical model based on a physical analysis of charge locations. IEEE 33rd annual power electronics specialists conference, vol. 3.
[31] Brown J. Modeling the switching performance of a MOSFET in the high side of a non-isolated buck converter. IEEE Trans Power Electron 2006;21(1):3–10.
[32] Maniktala S. Switching power supplies: A to Z. 2nd ed. Newnes; 2006.
[33] ANSYS HFSS <http://www.ansys.com/Products/Electronics/ANSYS-HFSS>.